CrystEngComm

PAPER

View Article Online
View Journal | View Issue

Cite this: *CrystEngComm*, 2017, **19**, 4287

Nanoporous carbon leading to the high performance of a $Na_3V_2O_2(PO_4)_2F$@carbon/graphene cathode in a sodium ion battery†

Hongyun Jin, ‡[a] Min Liu,‡[a] Evan Uchaker,[b] Jie Dong,[a] Qifeng Zhang,[b] Shuen Hou,[a] Jiangyu Li [c] and Guozhong Cao *[b]

Received 19th April 2017,
Accepted 19th June 2017

DOI: 10.1039/c7ce00726d

rsc.li/crystengcomm

The $Na_3V_2O_2(PO_4)_2F$/graphene sandwich cathode has attracted great attention as a potential candidate for sodium-ion batteries in view of its high capacity and good cycling ability. However, a big issue for $Na_3V_2O_2(PO_4)_2F$/graphene is its extremely poor electronic conductivity due to the multilayer structure in which $Na_3V_2O_2(PO_4)_2F$ particles are located between the graphene layers. We introduced carbon in the $Na_3V_2O_2(PO_4)_2F$/graphene sandwich to form a 3D architecture – $Na_3V_2O_2(PO_4)_2F$@carbon/graphene (NVPF@C/G). A battery with the NVPF@C/G cathode presents good electrochemical properties, a high capacity, 135.8 mAh g^{-1} at 0.1C, with a capacity retention of 96.8% at 2C for fifty cycles. NVPF@C/G showed obvious advantage in the rate performance and cycle stability compared with the NVPF/G sandwich, which indicated that the nanoporous carbon integrated in the 3D structure plays a crucial role in improving the electrochemical performance. It is anticipated that such a new method of introducing nanoporous carbon for battery performance enhancement can be extended to other graphene-based sandwich structure electrodes.

Introduction

For large-scale energy storage systems, lithium ion batteries (LIBs) have been well developed and considered as one of the most promising candidates because of their outstanding energy and power densities.[1–7] However, their large-scale application has encountered the challenge of limited lithium resources, which would lead to their high cost and limited applications.[8–10] As a consequence, sodium ion batteries (SIBs) have drawn increasing attention due to the earth abundance of resources, ease of accessibility, low cost and similar charge–discharge characteristics compared to LIBs.[11–14] Consequently, various cathode materials for SIBs, such as layered structure oxides,[15,16] NASICON framework compounds,[17,18] sodium vanadium fluorophosphates,[19,20] sodium iron–manganese fluorophosphates,[21,22] and Prussian blue analogues,[23,24] were developed. However, due to the larger radius of Na^+ (97 nm) than that of Li^+ (68 nm), it is more difficult for Na^+ to diffuse in/out of the electrode material, resulting in inferior electrochemical characteristics.[25,26] Many methods have been proposed and explored to circumvent this challenge. Out of the possible technical solutions available, introducing various carbon forms on cathode materials has been recognized as a propitious and effective approach to improve the electrical conductivity and electrochemical performance of SIBs.[17,27–33]

Song *et al.* reported that the use of a $Na_3V_2(PO_4)_2F_3$ and amorphous carbon composite as an SIB cathode delivered a capacity of 111.5 mAh g^{-1} with three discharge plateaus.[34] Jian *et al.* synthesized $Na_3V_2(PO_4)_3$/C samples, and confirmed that the appropriate carbon content was a key factor for the battery to gain good reversibility and excellent rate performance.[35] Duan *et al.* obtained a $Na_3V_2(PO_4)_3$@C core–shell nano-composite, showing good cycle life and rate capability.[36] Serras *et al.* reported a mixed-valence sodium vanadium fluorophosphate – $Na_3V_2O_{2x}(PO_4)_2F_{3-2x}$/C – that delivered 80 mAh g^{-1} at 1C, which is about 61.5% of its theoretical capacity.[37] Serras *et al.* also synthesized $Na_3(VO)_2(PO_4)_2F$ by *ex situ* carbon coating, which delivered a capacity of 68 mAh g^{-1} at 1C, about a half of its theoretical capacity.[38] This suggests that a carbon coating structure is effective in improving the battery performance to some extent; yet the rate performance and cycle life of the cathode material in SIBs are still unsatisfactory.

Graphene, due to its high electronic conductivity, is highly expected to resolve the predicament.[39–41] Jung *et al.* reported

[a] *Faculty of Materials Science & Chemistry, China University of Geosciences, Wuhan, 430074, China*
[b] *Department of Materials Science & Engineering, University of Washington, Seattle, WA, 98195, USA*
[c] *Department of Mechanical Engineering, University of Washington, Seattle, WA, 98195, USA*

† Electronic supplementary information (ESI) available. See DOI: 10.1039/c7ce00726d

‡ These authors contributed equally to the work.

a $Na_3V_2(PO_4)_3$/graphene composite as a cathode material for SIBs, delivering around 67% of the initial 0.2C capacity at a 30C rate.[39] Through a solvothermal method, Xu *et al.* employed graphene to modify $Na_3V_2O_2(PO_4)_2F$ and achieved a high capacity of 100.4 mAh g^{-1} at 1C, almost 77.2% of its theoretical capacity, while the discharge capacity at 10C is below 50 mAh g^{-1}.[42] Mai discussed $Na_3V_2(PO_4)_3$ battery performance in three carbon architectures, and revealed that $Na_3V_2(PO_4)_3$ dispersed in acetylene carbon nanospheres performed the best while that in graphene nanosheets gave the worst SIB performance.[43] This means the high-conductivity of graphene is really beneficial for improving battery performance, but it does not always guarantee the improvement of the electrochemical behaviors. A partial reason is that the conductivity of multilayer particles located between graphene layers is extremely poor and it becomes a crucial issue in graphene-based sandwich structures, which limits the battery performance.

So, it is a big challenge to fundamentally improve the overall conductivity of the $Na_3(VO)_2(PO_4)_2F$ cathode material. Recently, we reported a 3D architecture constructed from carbon wrapped multilayer $Na_3V_2O_2(PO_4)_2F$ nanocubes embedded in graphene (NVPF@C/G), which showed good electrochemical performance.[44] However, the detailed difference in introducing graphene and carbon was not researched systematically. In addition, the answers to some fundamental questions, such as 'How does nanoporous carbon improve the electrochemical behaviors?', 'What are the roles of carbon and graphene?', and 'What are the electron and Na^+ diffusion pathways?', are not very clear.

To have a definite answer to the above mysteries, $Na_3V_2O_2(PO_4)_2F$ (NVPF), $Na_3V_2O_2(PO_4)_2F$/graphene (NVPF/G) and $Na_3V_2O_2(PO_4)_2F$@carbon/graphene (NVPF@C/G) were prepared. The electrochemical behaviors of the three samples as a cathode in a sodium half-cell configuration are compared, revealing that NVPF@C/G possesses superior discharge capacities of 135.8 mAh g^{-1} and 102.1 mAh g^{-1} at 0.1C and 2C, the top capacity retention of 96.8% at 2C for fifty cycles (NVPF/G 85.8%, NVPF 50.2%) and the best rate performance (delivering around 70% of the 1C capacity at a 10C rate) compared to the NVPF/G sandwich structure and the NVPF sample.

Experimental section

Synthesis

NVPF, NVPF/G, NVPF@C/G materials were prepared by a similar process. Firstly, 2 mmol of $NH_4H_2PO_4$ (Sigma-Aldrich, 99.9% purity), 2 mmol of NH_4VO_3 (Sigma-Aldrich, 99.99% purity), 1 mmol of NaF (Sigma-Aldrich, 99%) and 1 mmol of Na_2CO_3 (Sigma-Aldrich, 99.9% purity) were separately dissolved in 5 mL of distilled water. Then these four precursor solutions were added to 50 mL of an *N*,*N*-dimethyl formamide (DMF) solution, and stirred for 30 minutes at 90 °C. After obtaining a homogeneous solution, it was sealed in a 100 mL capacity polytetrafluoroethylene (PTFE)-lined stainless-steel autoclave and was maintained at 180 °C for 24 hours, and then naturally cooled to room temperature. After washing repeatedly with distilled water and ethanol, NVPF was obtained. To obtain NVPF/G, graphene oxide, synthesized with a modified Hummers method, was immersed in 50 mL of DMF and ultrasonically treated for 24 hours. Then, $NH_4H_2PO_4$, NH_4VO_3, NaF and Na_2CO_3 in the same chemical ratios were separately dissolved in 5 mL of distilled water and added to the DMF, repeating the subsequent operations. As for NVPF@C/G, 50 mg of the NVPF/G was dissolved in distilled water and stirred for 30 min, then 12 mg of sucrose was added into the suspension under vigorous stirring and heating at 105 °C until it was dried. The powder mixture was ground and annealed at 550 °C for 1 h in a flowing argon atmosphere.

Characterization

Structure characterization. The morphology of the samples was examined by scanning electron microscopy (SEM, JEOL JSM-7000F) and high resolution transmission electron microscopy (HR-TEM, FEI Tecnai G20). X-ray diffraction (XRD, D8 Bruker X-ray diffractometer) was used to characterize the phase change of samples with Cu-Kα radiation within the range from 10° to 70° (2θ) and a step size of 0.02°. The accelerating voltage and current were 40 kV and 40 mA, respectively. Raman spectroscopy was carried out in a Thermo-Fisher Scientific Inc 5225 Verona Rd (USA) with a laser wavelength and the spectra were collected in the range of 1100–1900 cm^{-1}. The carbon content was analysed *via* a thermogravimetric differential scanning calorimeter (TG-DSC) (STA449C/3/G) with a heating rate of 10 °C min^{-1} in air.

Electrochemical analysis. For electrochemical analysis, 2016-type half-cells were assembled in a glove box (Mbraun) filled with high purity argon. The cathode was manufactured by mixing a slurry of the active material (75% wt), Super P conductive carbon (Timcal) (20% wt) and 5% PVDF binder in an *N*-methyl pyrrolidine (NMP) solvent. Then it was coated onto an aluminum foil current collector and dried at 80 °C for 12 h in a vacuum oven. Sodium metal (Sigma Aldrich) was used as an anode and 1 M $NaClO_4$ in ethylene carbonate (EC)/dimethyl carbonate (DMC) (1 : 1 v/v) and a glass fiber were used as the electrolyte, counter/reference electrode, and separator for the Na-ion half-cells, respectively. Cyclic voltammetry was performed using an electrochemical analyzer (CH Instruments, Model 605C). It was carried out between 2.0 and 4.3 V *vs.* Na/Na^+ at scanning rates ranging from 0.1 to 0.8 mV s^{-1}. The current density and cycle stability were determined using an Arbin Battery Tester (BT-2000, Arbin Instruments) between 2.0 and 4.3 V *vs.* Na/Na^+ at various charging rates and assuming 1C = 130 mA g^{-1}. Capacity values were normalized to the mass of NVPF, NVPF@C and NVPF@C/G. To validate the electrochemical kinetics of the NVPF series of electrode materials for sodium-ion half cells, electrochemical impedance spectroscopy (EIS) measurements were carried out in the frequency range from 100 kHz to 0.01

Hz with an AC signal amplitude of 10.0 mV and using a frequency response analyser (Solartron, 1260).

Results and discussion

Scanning electron microscopy (SEM) and transmission electron microscopy (TEM) were carried out to characterize the morphology and microstructure of the as-synthesized NVPF samples. In Fig. 1(a), it can be observed that the NVPF cuboids possess a typical diameter of 500 nm and length of about 1.5 μm. Some cuboids self-assembled to form flower-like aggregates. The SEM image of NVPF/G is shown in Fig. S1.† It reveals that the NVPF@G possesses a layered structure, as shown from various perspectives. Multiple layers of NVPF cubes stack between the parallel graphene sheets. NVPF/G nanocubes about 200 nm as shown in Fig. 1(b) were observed. The size of NVPF/G nanocubes is much smaller than that of the bare NVPF cuboids, likely suggesting that their growth along the [001] direction has been restricted by graphene. Fig. 1(c) reveals that NVPF@C/G has a typical multilayer structure and the NVPF particles are connected to each other through carbon coating and are embedded into graphene layers, looking like the NVPF particles are rooted on the graphene layers. As shown in Fig. 1(c), few cuboids outside of the layers were found, which further proves that carbon and graphene can limit the NVPF growth along the [001] direction. The high magnification TEM image shown in Fig. 1(d) clearly shows that the NVPF cubes with the size of approximately 200 nm are grasped by both graphene and carbon. There is no obvious difference in the morphology and size compared to the NVPF/G sample shown in Fig. 1(b), except that a thin layer of carbon coating was observed for NVPF/G. In other words, the carbon coating prevented the nanocubes from growing big under a short annealing time. Compared to the raw NVPF sample, the dispersibility of NVPF@C/G has been significantly improved, which shows evidence that the carbon may suppress the NVPF from aggregating during the annealing process. By further magnifying a sample, it is observed in Fig. 1(e) that the carbon coating wrapped a NVPF particle. The carbon has a porous structure and its thickness is around 5 nm. The homogeneous porous carbon coating structure can limit the volume change of NVPF materials and keep the NVPF electrode stable during Na^+ intercalation and deintercalation.[41] Moreover, the porous carbon coating may enhance Na^+'s diffusion ability[31] and thus improve the electrochemical performance of a battery. Fig. 1(f) is the magnified image of Fig. 1(e). It can be seen that the lattice spacing value is 0.45 nm, corresponding to the NVPF (110) facet. Besides, we notice that the porous carbon is wrapped on the NVPF particles and the pore size was not very clear. Since we cannot obtain the information from the high-resolution diffraction image in Fig. 1(f), likely it means the carbon is amorphous. Such a thin amorphous carbon coating plus the nanoporous structure may facilitate the electrolyte diffusion and sodium ion transport. Meanwhile, the carbon coating bridges the nanocubes and graphene, giving rise to a remarkable improvement in the conductivity of the NVPF electrode.

X-ray diffraction patterns (XRD) of the as-prepared NVPF@C/G, NVPF/G, and raw NVPF are presented in Fig. 2. All the diffraction patterns of the three samples fit well with the standard pattern for tetragonal $Na_3V_2O_2(PO_4)_2F$ (PDF No: 01-076-3645). No other peaks from impurities were detected,

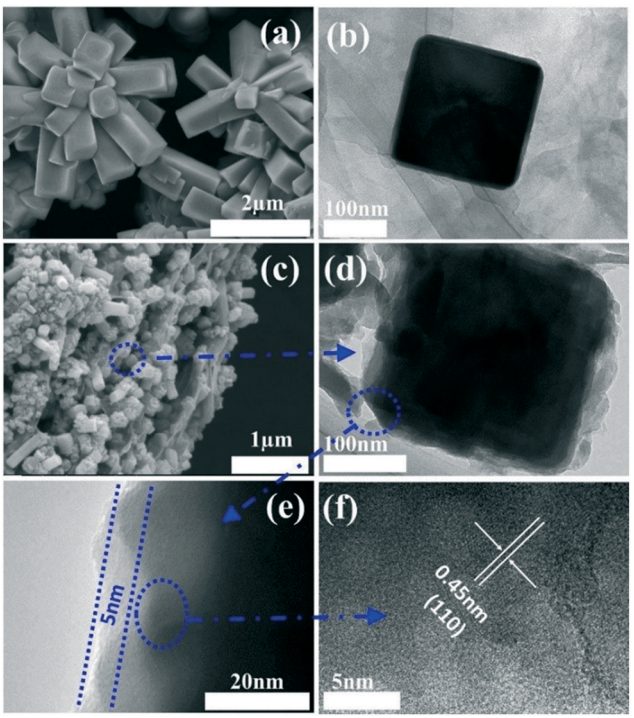

Fig. 1 SEM and TEM images of NVPF series of specimens: (a) low magnification SEM image of bare NVPF; (b) TEM image of NVPF/G; (c) overall views of NVPF@C/G; (d) a typically multilayered NVPF@C/G cube between graphene layers; (e) TEM image of NVPF@C/G and nanoporous carbon; (f) HRTEM image of NVPF@C/G.

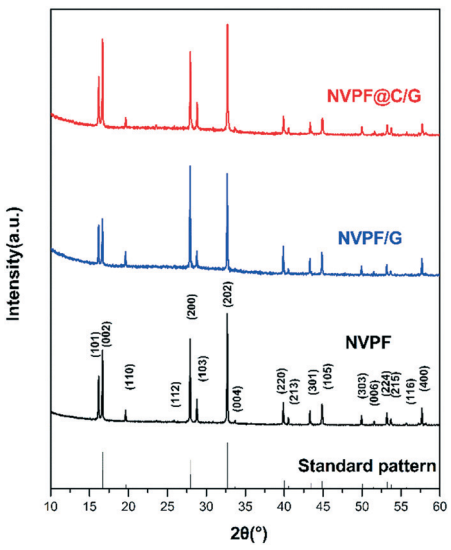

Fig. 2 XRD patterns of NVPF series of samples.

which indicates that the as-synthesized samples are of pure phase of crystalline NVPF.[45] On the XRD pattern of NVPF@C/G, a weak diffraction peak around $2\theta \approx 23°$ is observed. It probably corresponds to the reduced graphene phase.[46] Based on the fact that we observed the carbon wrapping on NVPF particles from the SEM and TEM images in Fig. 1, however, characteristic peaks of carbon were not found. We suggest that porous carbon is amorphous derived from sucrose.[47] In other words, introducing graphene and carbon does not affect the structure of NVPF. To certify the existence of graphene and carbon, Raman spectroscopy was used to test the NVPF@C/G sample, and the curves are shown in Fig. S2.† From the Raman spectra in Fig. S2,† the D and G bands appeared at 1340 cm^{-1} and 1580 cm^{-1}, which can be assigned to typical D and G bands of the carbon materials, respectively. The D band originated from defects associated with vacancies and amorphous carbon species and the G band corresponded to ordered sp^2 bonded carbon atoms.[48] And the Raman intensity of the D band is close to the G band, which indicates the high quality of the graphene and carbon that composed the sample. To further confirm the carbon content in NVPF@C/G, the TG of NVPF@G and NVPF@C/G was characterized, as shown in Fig. S3.† We can see that the total weight loss is 2.6% and 12% for the two samples, respectively, in which 2% and 1.8% water weight loss was included. Thus, the carbon weight is 0.6% and 10.2% for NVPF@G and NVPF@C/G, respectively.

Fig. 3(a) exhibits the rate capacities of bare NVPF, NVPF/G and NVPF@C/G samples at different charge–discharge rates. In general, NVPF@C/G gives the highest discharge capacity, NVPF/G is at medium capacity, and bare NVPF presents the lowest one at all rates. For NVPF@C/G, the specific discharge capacities are 135.8, 123.8, 113.4, 90.9, 78.2 mAh g^{-1} at 0.1C, 0.5C, 1C, 5C and 20C, respectively. To our knowledge, compared to the values reported, the present discharge capacities are the best. The improved capacities are likely attributed to the hybrid structure consisting of carbon-coated nano-scale cubes embedded into graphene sheets, which greatly promotes sodium-ion storage as well as electrochemical activation during the charge–discharge process.[49,50] Furthermore, the capacity gap between various rates for NVPF@C/G is the narrowest compared to the other two samples, which suggests that NVPF@C/G has the best high-rate performance. For NVPF, it seems that the relatively big size of particles is a disadvantageous factor for electron transport.[51] Comparing NVPF@C/G and NVPF/G, which have a similar particle morphology and size, it can be seen that the rate performance is obviously different, especially at a higher rate. This is probably due to the porous carbon coating in NVPF@C/G, which can keep the NVPF structure stable even under a high current-density charge–discharge process. In addition, the porous carbon can provide more space for volume change taking place during the charge–discharge process, and thus improve the cycling ability. To better evaluate the high-rate performance of electrode materials, we tested the cycle performance of the three samples at 2C in 2.0–4.3 V for 50 cycles. The results are displayed in Fig. 3(b). For NVPF@C/G, the initial discharge capacity is 102.1 mAh g^{-1} and it maintains at 98.8 mAh g^{-1} after 50 cycles; the capacity retention is about 96.8%. However, for NVPF/G, the initial discharge capacity is 75.6 mAh g^{-1} and it decreases to 64.9 mAh g^{-1} after 50 cycles; the capacity retention is about 85.8%. At a higher current density, the transporting of sodium ions is more difficult basically, even more for graphene composites.[52] This remarkable difference can be attributed to the thin carbon coating combined with graphene sheet, which tether the NVPF particles, embed particles on the sheets, and keep the space among particles to promote sodium ions' diffusion. Such similar results have been reported.[49] In Fig. S4,† we can see that the coulombic efficiency of NVPF@C/G is always close to 100% during the cycling tests, whereas the coulombic efficiency for NVPF/G has a little fluctuation. It indicates that NVPF@C/G has better reversibility, thanks to the unique carbon coating which makes the NVPF more stable during the Na^+ intercalation and deintercalation process.

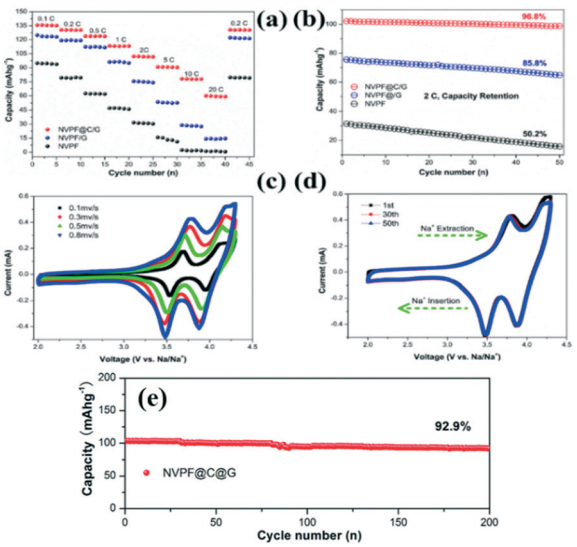

Fig. 3 The electrochemical properties and CV curves of NVPF series of specimens: (a) rate performance of NVPF@C/G in comparison with homemade NVPF/G and bare NVPF; (b) discharge capacity retention at 2C for NVPF@C/G, NVPF/G and NVPF in 2.0–4.3 V for 50 cycles; (c) CV curves of NVPF@C/G at a scanning rate from 0.1–0.8 mV s^{-1} over the voltage range of 2.0–4.3 V *vs.* Na/Na^+; (d) the first 50th CV curves of NVPF@C/G tested at 0.8 mV s^{-1} between 2.0–4.3 V *vs.* Na/Na^+ and (e) discharge capacity retention at 2C in 2.0–4.3 V for 200 cycles for NVPF@C/G.

To better understand the extraction and insertion mechanism of Na ions during the charge–discharge process, cyclic voltammetry (CV) measurement was carried out. The CV curves (between 2.0–4.3 V) at various scanning rates (ranging from 0.1–0.8 mV s^{-1}) are depicted in Fig. 3(c), in which a couple of nearly reversible redox peaks are found. The NVPF@C/G electrode material used in SIBs for the first cycle displayed two obvious anodic peaks located at 3.69 V and 4.12 V *vs.* Na^+/Na, which proves that two sodium ions were released; in other words, $Na_3V_2O_2(PO_4)_2F$ transformed to $NaV_2O_2(PO_4)_2F$ in the charge process.[53] Conversely, two cathodic peaks

located at 3.54 and 3.95 V *vs.* Na^+/Na are observed, implying two sodium ions were inserted, resulting in the reduction of V^{5+} to V^{4+} in the discharge process. In addition, the hysteretic voltages are 0.15 V and 0.17 V, respectively, between the two couples of redox peaks, in which the minor values determine the excellent reversibility of NVPF@C/G. In Fig. 3(c), both anodic peaks float to higher voltages about 0.6 V. Meanwhile, the two cathodic peaks in the discharge curves shift towards the left about 0.6 V when the scanning rate is raised from 0.1 to 0.8 mV s^{-1}. Moreover, both the values of the current peaks become larger with an increase in the scanning rate from 0.1 to 0.8 mV s^{-1}. These results are in agreement with those previous literature reports.[54] A comparison of the CV curves corresponding to the first, 30th and 50th cycles are displayed in Fig. 3(d). Although the anodic peaks shift a little to higher voltages after 30 or 50 cycles in the charge stage (while cathodic peaks keep almost unchanged), in general, the three CV curves seem the same, which certifies that wrapping carbon on NVPF particles and embedding the NVPF@C structure into graphene sheets can limit the volume change and keep the NVPF crystal structure stable during sodium ions' intercalation and deintercalation. To confirm the long-term cycling stability and high rate capability of NVPF@C/G as a cathode material for sodium ion batteries, it was tested at an extremely high specific current of 2C for 200 cycles shown in Fig. 3(e). We can observe that the discharge capacity stabilized at around 92.8 mAh g^{-1} and the capacity retention was about 92.9% after the 200th cycle. In a word, the reasons for improved electrochemical performances, especially the cycling stability, could be attributed to carbon nano-coating which can effectively improve the structural stability of the electrode by suppressing aggregation of NVPF@G and accommodating their volume expansion during electrochemical cycling.[55,56] These results indicate that NVPF@C/G is an ideal electrode material which can be used for sodium ion batteries to bring about remarkably good reversibility and cycle stability.

Fig. 4 presents the Nyquist plots of the three samples activated at 0.05C after 2 cycles and the inset shows the equivalent circuit. The diameter of the semicircle at the high frequency region is attributed to the combined process of electron transport in the surface film and the charge transfer resistance.[30] In Fig. 4, NVPF@C/G depicts the lowest charge-transfer resistance compared to NVPF/G and NVPF (276 Ω *vs.* 513 Ω and 818 Ω). The transfer resistance of NVPF@C/G is nearly half of that of NVPF/G, which is attributed to the thin carbon coating that tethers the NVPF cubes and reduces the contact resistance among particles. Comparing NVPF/G and NVPF, the resistance decreases by approximately 37%, whereas between NVPF@C/G and NVPF/G, the drop-out value is close to 46%, which means carbon coating plays a critical role in the 3D architecture. Such a remarkable decrease of the R (R_1 + R_2) value indicates that NVPF@C/G has the best contact and the lowest charge-transfer resistance, suggesting the best sodium-ion insertion/extraction kinetics. The sloping line at the low frequencies is associated with the Warburg resistance originating from the solid-state diffusion of sodium-ions in the active materials.[57] The highest line sloping of NVPF@C/G means it has the best sodium ion diffusion efficiency, which suggested that the electrochemical reaction becomes easier compared to NVPF/G and NVPF. This observation highly supports the explanation for the better rate performance of the half cells using the NVPF@C/G as a cathode material. From the impedance analysis, we can draw a conclusion that the graphene improves the conductivity of the NVPF electrode materials, while the porous carbon further makes the transfer of both sodium ions and electrons faster during the cycling process. Moreover, the microstructures of the cycled cathode materials were investigated by SEM, as shown in Fig. S5.† It can be seen that the morphology and structure of NVPF@C/G change a little after 50 cycles at 2C current, demonstrating that carbon nano-coating could effectively improve the structural stability in this structure after long cycles, which is accorded with the high capacity retention, 96.8% after 50 cycles. Consequently, compared with the other two samples, the NVPF@C/G electrode material displays better rate performance, cyclic stability and reversible capability.

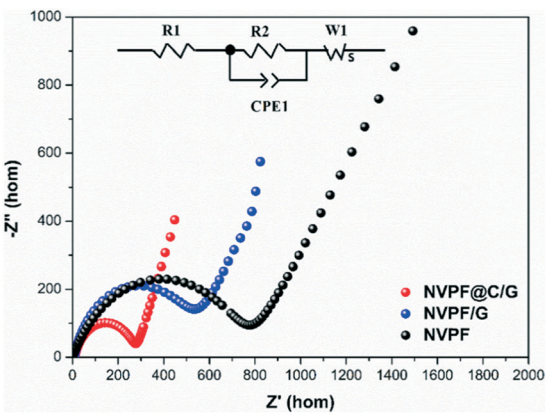

Fig. 4 Nyquist plots of NVPF@C/G in comparison with homemade NVPF/G and bare NVPF; inset depicts the equivalent circuit model.

For NVPF, due to its poor conductivity, electrons are difficult to transport on NVPF cubes basically. In Fig. 5(a), the high-conductivity graphene sheets in the graphene sandwich structure are like two parallel "expressways"; between them, there are no "interstates" to connect each other. For the particles in the middle of the multilayer's particle structure as seen in Fig. 5(a), the electrons pass through it with double difficulty, like on a "winding path". That means the "expressway" efficiency is significantly decreased. It is well known, for a sodium storage process, that it needs not only highly efficient electron transport but also fast sodium ion diffusion in the electrode material.[58] Therefore, the porous carbon "interstates" become especially important. As a consequence, we adopted homogeneous thin porous carbon to wrap NVPF particles as shown in Fig. 5(b). The porous carbon is suggested to work as a pathway to bridge the NVPF particles so that the electrons can be transported through the particles to

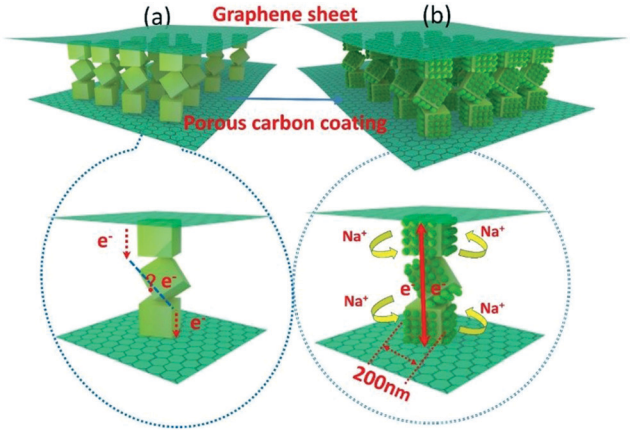

Fig. 5 Schematic illustration of electrons' transport and ions' diffusion in the 3D NVPF@C/G architecture: (a) without carbon bridge; and (b) with carbon bridge.

graphene sheets with high efficiency. This could explain why the rate performance and cycle stability of NVPF@C/G are obviously improved compared to NVPF/G. Also Fig. 5(b) shows an open 3D structure, which is beneficial for electrolyte diffusion and sodium ion transport. On one hand, the inclusion of carbon and graphene hinders the NVPF particles from growing bigger, thus it can shorten the electron transport length and thus accelerate oxidation reduction reactions. On the other hand, carbon and graphene reduce the agglomeration between the particles, which is beneficial for the contact between active materials and the electrolyte. The 3D architecture also makes the NVPF structure stable during the Na^+ insertion and extraction process. On one side, NVPF particles *in situ* pillared with graphene mean the particles would be embedded into graphene sheets, which can limit the volume change. Moreover, the thin carbon coating tightly wraps on the surface of particles, which can also prevent the collapse of the NVPF structure during the long cycle process. Furthermore, the porous carbon structure can largely increase the contact area between the electrode and electrolyte, which effectively facilitates the sodium ion diffusion kinetics. In brief, the nanosized particles, open structure, thin and homogeneous porous carbon coating, highly conductive graphene sheets, and 3D architecture jointly contribute to yielding highly effective ambipolar diffusion of sodium ions and electrons into/out NVPF, giving rise to good rate performance and long cycling lifetime.

Conclusion

A 3D architecture – the NVPF@C/G structure – as a cathode material for SIBs was synthesized and its electrochemical properties were compared with NVPF/G and bare NVPF samples. NVPF@C/G possesses the highest discharge capacities, 135.8 mAh g^{-1} at 0.1C, the best cyclic stability, and an excellent capacity retention, 96.8% at 2C for fifty cycles. The obvious difference in the electrochemical behaviors of NVPF@C/G and NVPF/G demonstrates that the porous carbon plays a key role in bridging the NVPF particles in the multilayer particle structure, in which electrons can transport through the NVPF particles efficiently to facilitate the sodium ion diffusion kinetics. In addition, the porous carbon can effectively enhance the structural stability of the NVPF during the sodium-ion insertion–extraction process. Therefore, while graphene has been well recognized as an additive that can increase the conductivity of an electrode material, the use of porous carbon to bridge the NVPF particles and graphene as discussed in this paper is another both facile and effective method to further enhance the conductivity of the electrode material and to thus improve the electrochemical performance of SIBs.

Acknowledgements

Part of this work was financially supported in part by the financial support from the National Key Research and Development Program of China (2016YFA0201001), the National Science Foundation (NSF, DMR-1505902), and the National Natural Science Foundation of China (NSFC51102218, 11627801).

Notes and references

1 M. Armand and J.-M. Tarascon, *Nature*, 2008, **451**, 652–657.
2 J. W. Choi and D. Aurbach, *Nat. Rev. Mater.*, 2016, **1**, 16013.
3 J. Lee, A. Urban, X. Li, D. Su, G. Hautier and G. Ceder, *Science*, 2014, **343**, 519–522.
4 M. Sathiya, G. Rousse, K. Ramesha, C. Laisa, H. Vezin, M. T. Sougrati, M.-L. Doublet, D. Foix, D. Gonbeau and W. Walker, *Nat. Mater.*, 2013, **12**, 827–835.
5 A. Urban, J. Lee and G. Ceder, *Adv. Energy Mater.*, 2014, **4**, 1400478.
6 C. Liu, R. Massé, X. Nan and G. Cao, *Energy Storage Materials*, 2016, **4**, 15–58.
7 B. Dunn, H. Kamath and J.-M. Tarascon, *Science*, 2011, **334**, 928–935.
8 E. C. Evarts, *Nature*, 2015, **526**, S93–S95.
9 E. Uchaker, Y. Zheng, S. Li, S. Candelaria, S. Hu and G. Cao, *J. Mater. Chem. A*, 2014, **2**, 18208–18214.
10 J. Qian, X. Wu, Y. Cao, X. Ai and H. Yang, *Angew. Chem.*, 2013, **125**, 4731–4734.
11 Z. Ma, Y. Wang, C. Sun, J. Alonso, M. Fernández-Díaz and L. Chen, *Sci. Rep.*, 2014, **4**, 7231.
12 Y. You, X.-L. Wu, Y.-X. Yin and Y.-G. Guo, *Energy Environ. Sci.*, 2014, **7**, 1643–1647.
13 Y. S. Yun, K. Y. Park, B. Lee, S. Y. Cho, Y. U. Park, S. J. Hong, B. H. Kim, H. Gwon, H. Kim and S. Lee, *Adv. Mater.*, 2015, **27**, 6914–6921.
14 R. C. Massé, E. Uchaker and G. Cao, *Sci. China Mater.*, 2015, **58**, 715–766.
15 D. Kim, E. Lee, M. Slater, W. Lu, S. Rood and C. S. Johnson, *Electrochem. Commun.*, 2012, **18**, 66–69.
16 P. Senguttuvan, G. Rousse, V. Seznec, J.-M. Tarascon and M. R. Palacin, *Chem. Mater.*, 2011, **23**, 4109–4111.
17 Y. Fang, L. Xiao, X. Ai, Y. Cao and H. Yang, *Adv. Mater.*, 2015, **27**, 5895–5900.

18 H. Li, Y. Bai, F. Wu, Y. Li and C. Wu, *J. Power Sources*, 2015, **273**, 784–792.
19 V. Palomares, P. Serras, H. Brand, T. Rojo and N. Sharma, *J. Mater. Chem. A*, 2015, **3**, 23017–23027.
20 M. Peng, B. Li, H. Yan, D. Zhang, X. Wang, D. Xia and G. Guo, *Angew. Chem., Int. Ed.*, 2015, **54**, 6452–6456.
21 Y. Kawabe, N. Yabuuchi, M. Kajiyama, N. Fukuhara, T. Inamasu, R. Okuyama, I. Nakai and S. Komaba, *Electrochemistry*, 2012, **80**, 80–84.
22 S. M. Wood, C. Eames, E. Kendrick and M. S. Islam, *J. Phys. Chem. C*, 2015, **119**, 15935–15941.
23 Y. Lu, L. Wang, J. Cheng and J. B. Goodenough, *Chem. Commun.*, 2012, **48**, 6544–6546.
24 Y. Yue, A. J. Binder, B. Guo, Z. Zhang, Z. A. Qiao, C. Tian and S. Dai, *Angew. Chem.*, 2014, **126**, 3198–3201.
25 B. L. Ellis and L. F. Nazar, *Curr. Opin. Solid State Mater. Sci.*, 2012, **16**, 168–177.
26 H. Pan, Y.-S. Hu and L. Chen, *Energy Environ. Sci.*, 2013, **6**, 2338–2360.
27 A. C. Ferrari, F. Bonaccorso, V. Fal'Ko, K. S. Novoselov, S. Roche, P. Bøggild, S. Borini, F. H. Koppens, V. Palermo and N. Pugno, *Nanoscale*, 2015, **7**, 4598–4810.
28 J. Liu, K. Tang, K. Song, P. A. van Aken, Y. Yu and J. Maier, *Nanoscale*, 2014, **6**, 5081–5086.
29 G. Longoni, J. E. Wang, Y. H. Jung, D. K. Kim, C. M. Mari and R. Ruffo, *J. Power Sources*, 2016, **302**, 61–69.
30 Y. Lu, S. Zhang, Y. Li, L. Xue, G. Xu and X. Zhang, *J. Power Sources*, 2014, **247**, 770–777.
31 C. Zhu, K. Song, P. A. van Aken, J. Maier and Y. Yu, *Nano Lett.*, 2014, **14**, 2175–2180.
32 Y. Shao, J. Xiao, W. Wang, M. Engelhard, X. Chen, Z. Nie, M. Gu, L. V. Saraf, G. Exarhos and J.-G. Zhang, *Nano Lett.*, 2013, **13**, 3909–3914.
33 J. Xie, X. Yao, Q. Cheng, I. P. Madden, P. Dornath, C. C. Chang, W. Fan and D. Wang, *Angew. Chem.*, 2015, **127**, 4373–4377.
34 W. Song, X. Ji, Z. Wu, Y. Zhu, F. Li, Y. Yao and C. E. Banks, *RSC Adv.*, 2014, **4**, 11375–11383.
35 Z. Jian, L. Zhao, H. Pan, Y.-S. Hu, H. Li, W. Chen and L. Chen, *Electrochem. Commun.*, 2012, **14**, 86–89.
36 W. Duan, Z. Zhu, H. Li, Z. Hu, K. Zhang, F. Cheng and J. Chen, *J. Mater. Chem. A*, 2014, **2**, 8668–8675.
37 P. Serras, V. Palomares, A. Goñi, I. G. de Muro, P. Kubiak, L. Lezama and T. Rojo, *J. Mater. Chem.*, 2012, **22**, 22301–22308.
38 P. Serras, V. Palomares, P. Kubiak, L. Lezama and T. Rojo, *Electrochem. Commun.*, 2013, **34**, 344–347.
39 Y. H. Jung, C. H. Lim and D. K. Kim, *J. Mater. Chem. A*, 2013, **1**, 11350–11354.
40 R. Raccichini, A. Varzi, S. Passerini and B. Scrosati, *Nat. Mater.*, 2015, **14**, 271–279.
41 W. Xu, Z. Xie, X. Cui, K. Zhao, L. Zhang, G. Dietrich, K. M. Dooley and Y. Wang, *ACS Appl. Mater. Interfaces*, 2015, **7**, 22533–22541.
42 M. Xu, P. Xiao, S. Stauffer, J. Song, G. Henkelman and J. B. Goodenough, *Chem. Mater.*, 2014, **26**, 3089–3097.
43 S. Li, Y. Dong, L. Xu, X. Xu, L. He and L. Mai, *Adv. Mater.*, 2014, **26**, 3545–3553.
44 H. Jin, J. Dong, E. Uchaker, Q. Zhang, X. Zhou, S. Hou, J. Li and G. Cao, *J. Mater. Chem. A*, 2015, **3**, 17563–17568.
45 M. Xu, L. Wang, X. Zhao, J. Song, H. Xie, Y. Lu and J. B. Goodenough, *Phys. Chem. Chem. Phys.*, 2013, **15**, 13032–13037.
46 H. J. Shin, K. K. Kim, A. Benayad, S. M. Yoon, H. K. Park, I. S. Jung, M. H. Jin, H. K. Jeong, J. M. Kim and J. Y. Choi, *Adv. Funct. Mater.*, 2009, **19**, 1987–1992.
47 S. Hu, W. Chen, E. Uchaker, J. Zhou and G. Cao, *Chem. – Eur. J.*, 2015, **21**, 18248–18257.
48 X. Jiang, X. Yang, Y. Zhu, Y. Yao, P. Zhao and C. Li, *J. Mater. Chem. A*, 2015, **3**, 2361–2369.
49 K. Han, Z. Liu, J. Shen, Y. Lin, F. Dai and H. Ye, *Adv. Funct. Mater.*, 2015, **25**, 455–463.
50 R. Raccichini, A. Varzi, S. Passerini and B. Scrosati, *Nat. Mater.*, 2015, **14**, 271–279.
51 L. Shen, E. Uchaker, X. Zhang and G. Cao, *Adv. Mater.*, 2012, **24**, 6502–6506.
52 F.-Y. Su, Y.-B. He, B. Li, X.-C. Chen, C.-H. You, W. Wei, W. Lv, Q.-H. Yang and F. Kang, *Nano Energy*, 2012, **1**, 429–439.
53 Y. U. Park, D. H. Seo, H. Kim, J. Kim, S. Lee, B. Kim and K. Kang, *Adv. Funct. Mater.*, 2014, **24**, 4603–4614.
54 P. Serras, V. Palomares, A. Goñi, P. Kubiak and T. Rojo, *J. Power Sources*, 2013, **241**, 56–60.
55 C. Zhao, C. Yu, M. Zhang, H. Huang, S. Li, X. Han, Z. Liu, J. Yang, W. Xiao, J. Liang, X. Sun and J. Qiu, *Adv. Energy Mater.*, 2017, 1602880.
56 D. Xie, J. W. Tang, D. Y. Wang, H. X. Xia, Y. Zhou, D. H. X. L. Wang and J. P. Tu, *Nano Res.*, 2016, **9**, 1618–1629.
57 K. Feng, Y. Cheng, M. Wang, H. Zhang, X. Li and H. Zhang, *J. Mater. Chem. A*, 2015, **3**, 19469–19475.
58 Q. Wei, Q. An, D. Chen, L. Mai, S. Chen, Y. Zhao, K. M. Hercule, L. Xu, A. Minhas-Khan and Q. Zhang, *Nano Lett.*, 2014, **14**, 1042–1048.